Chapter 6

Tests of edgeless silicon sensors

6.1 Introduction

As explained in Chapter 1, our work on edgeless silicon sensors was motivated by the need for the measurement of the very forward elastic scattering at the CERN LHC (Large Hadron Collider). The forward scattering amplitude is needed in the luminosity-independent measurement of the total cross section [14][50], which also yields the value for the luminosity itself, enabling the calibration of luminosity monitoring detectors that are simpler, faster and operational at full luminosity.

The edgeless sensors are sensitive to minimum ionizing particles traversing the sensor up to its physical edge near the beam. If several sensors are placed symmetrically with respect to the interaction point so that the nearly parallel beams at the interaction point are focused to a point in the vertical plane of the detectors, the sensor can be placed at a minimal distance to the beam of $y_{min} = n \cdot \sigma_y$, where σ_y is the gaussian height of the beam at the focal point, and n ranges between 10 and 15. In the example of [50] the minimum vertical beam spot is smaller than $\sigma_y = 0.1$ mm on the detector, which yields the minimum scattering angle of

$$\theta_{\mathrm{cm}} \geq \frac{n\sigma_y}{L_{eff}} \cong 10 \mu\mathrm{rad} \tag{6.1}$$

at the upper limit of n. Here the effective distance L_{eff} is about 150 m, which is shorter than the physical distance from the interaction point to the detectors, and is determined by the beam optics in this part of the machine. The Equation 6.1 yields the minimum momentum transfer (t_{min}) of

$$t_{\mathrm{min}} = -4p^2\left(\sin\frac{\theta_{\mathrm{cm}}}{2}\right)^2 \cong -(p\theta_{\mathrm{cm}})^2 \cong -5 \cdot 10^{-3}\frac{\mathrm{GeV}^2}{c^2}, \tag{6.2}$$

measured at the full 7 TeV energy of LHC.

The vertical position resolution requirement of the detector follows from the vertical size of the beam at the detector, which is related with the beam divergence σ_θ^* at the interaction point in the previous example. This relation is simple in the case of parallel-to-point focusing and reads

$$\sigma_\theta^* = \frac{\sigma_y}{L_{eff}} \cong 0.7 \mu\mathrm{rad} \quad . \tag{6.3}$$

For best control of systematic errors related with the detectors, with the beam and with the experimental layout, the resolution should be in the range of $\Delta y = \sigma_y / m$, where m is between 3 and 10. Such a

consideration suggests that the vertical resolution of the sensor should be between 10 μm and 30 μm, which can be obtained with thin microstrip detectors using charge interpolation between the pixel or strip segments.

The edge sensitivity can be demonstrated in a simple way using silicon pad sensors. The shape of the electric field near the edge can be deformed by a high surface conductivity on a portion of the edge. The edge field will then be concentrated on the poorly conducting portion of the surface and therefore the charge signal will be collected only from this region . Such deformation of the electric field may reduce the charge signal close to the edge below the set threshold. In segmented sensors this would reduce the accuracy of the charge interpolation, which would degrade the efficiency and position resolution of the sensor upon approaching its physical edge.

A pair of edgeless silicon diode pad sensors, cut through their p^+ implant at BNL (Brookhaven National Laboratory) using dicing and chemical treatment techniques as described in [51], was exposed to the X5 high energy pion beam at CERN, to determine the edge sensitivity. The signal of the edgeless sensor pair triggered a reference telescope made of silicon microstrip detector modules. The processing of these devices is described in Section 6.2, and the layout of the experiment in the X5 beam area at CERN is shown in Section 6.3. The analysis of the experimental data is described in Section 6.4, before discussing the results in Section 6.5 and presenting the conclusions of the analysis in Section 6.6.

6.2 Edgeless silicon pad sensors

A high-resistivity silicon p^+-i-n^+ planar diode sensor, of 0.25 cm^2 active pad area, was diced through its front p^+ implant to produce two halves of edgeless diode pad sensors, as shown by Figure 6.1 The structure was manufactured at the Semiconductor Detector Development and Processing Laboratory of BNL, using a simple processing technology involving only three mask steps. The active pad is surrounded by a guard ring of 150 μm width, and the gap between the guard ring and the active pad is 100 μm. The distance between the guard ring and the original scribing line is 1.46 mm.

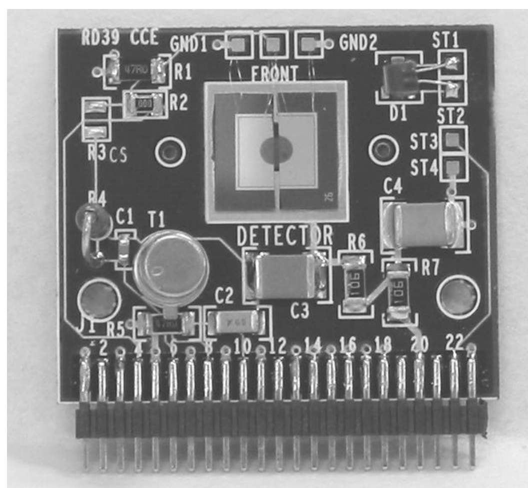

Figure 6.1 A pair of edgeless diodes mounted on a PCB where the gap of about 450 μm between the diodes can be observed.

In the recent work of the RD39 Collaboration [51], edgeless silicon sensors diced with laser cutting and scribing were characterized. It was found that with no chemical or aging treatment of the edge, all the sensors showed a very high leakage current (several hundred µA to a few mA) at full depletion potential, compared to a few nA before dicing. However, after one day of room temperature aging in air, the leakage current at full depletion potential decreased dramatically to 1 µA to 2 µA if diced from the backside either by laser cutting or by scribing. There was no breakdown up to 500 V bias potential, and after one day of aging the sensor showed normal *C-V* and charge collection behaviour. The remaining leakage current seemed to be dominated by surface current and showed little improvement at temperatures down to 130 K. There was little improvement over time for sensors diced from the front side.

For a normal sensor, the leakage current is dominated by that generated thermally in the bulk. This decreases exponentially with inverse temperature, and increases proportional to the number of active defects in the bulk. For laser diced edgeless sensors, the main component of the leakage current is the edge surface current, which is affected by surface defects rather than bulk defects. Although leakage currents for these edgeless sensors decrease with decreasing temperature, the rate of this decrease is much smaller and we measure values of 0.1 nA to 1 nA at 100 V bias and 90 K. Typical temperature dependences of leakage currents are shown in Figure 6.2. These curves cannot be explained using simple models involving a few thermal activation energies, and the temperature dependences vary substantially from one device to another.

Chemical treatment seems promising for further reduction of the surface current below 1 µA at full depletion potential and below 10 µA at 500 V. To do the etching, the sensors are coated with black wax on both sides to protect the sensitive area. The uncoated edge is then etched in an acid solution (HNO_3:HF(48%) = 3:1), with etching rate of about 15 µm/min at room temperature. Between 1 and 2 minutes is enough to remove cutting-caused defects completely. With chemical etching there is no difference if the sensor is scribed on the front side or on the back side. This is important, since to cut a non-straight pattern, one needs to cut it with laser all the way through.

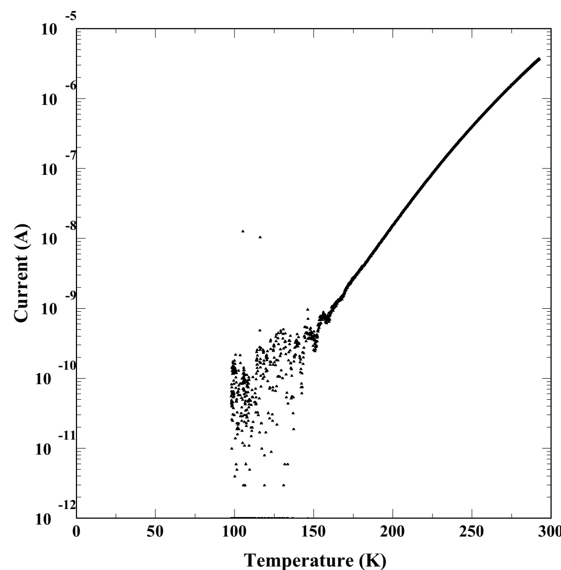

Figure 6.2 Leakage current of an edgeless diode as function of temperature, at 50 V reverse bias potential.

The current-voltage characteristics of our edgeless diode was measured at 300 K and at 90 K. At room temperature the leakage current was 400 nA at 10 V, while at low temperature was of a few nA at 200 V, as shown by Figure 6.3.

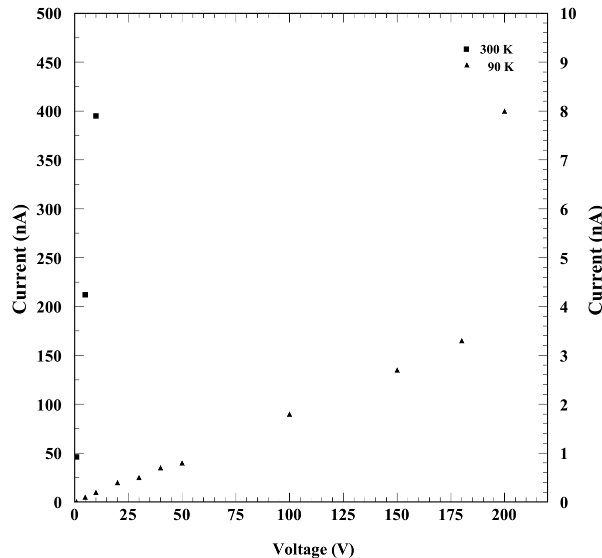

Figure 6.3 The *V-I* characteristic of the edgeless diode at room temperature (left scale) and at 90 K (right scale).

6.3 Experimental method and equipment

The goal of our tests was to determine the detection efficiency of the edgeless device as a function of the distance from the physical edge. Because the relative positions of a particle track and the physical edge of a sensor are hard to determine with high accuracy, two edgeless sensors were mounted so that a gap of about 450 µm was left between the processed edges, as shown by Figure 6.1. Using a reference tracker it is then easy to determine the width of the gap, by triggering the tracker with the discriminated charge signal of the pair of edgeless sensors. The track data can, in principle, be used to estimate both the average thickness of the possible dead layer at the edges of the sensors, and the possible gradual loss of efficiency when approaching the limit of the dead zone. In practice the tracker resolution limited the accuracy of the second, and the first remained the most accurate method for estimating the thickness of the dead zone. This will be discussed in detail in Section 4.

Special tooling was designed to glue the two edgeless diodes with a regular gap in between. Conductive Bipax Tra-con® conductive glue and Araldite® 2011 were used for biasing the sensor and for mechanical purposes, respectively. The gap between the diodes was measured by the Metrology service of CERN (Figure 6.4) at five points along the gap, with a precision of ±3 µm. From bottom to top, the gap widths measured at 293 K are 416, 410, 405, 460 and 484 µm. Some chipping could be observed in the top part of the diode, which is in agreement with the larger gap measured in that part.

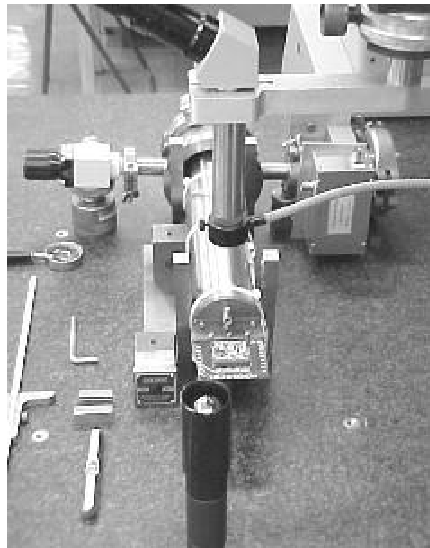

Figure 6.4 Metrology measurements of the gap width between the pair of edgeless diodes at the Metrology service at CERN.

This pair of edgeless silicon diode pad sensors was exposed for two weeks to a high energy pion beam of 120 GeV/c momentum in the X5 experimental area at CERN, in order to determine the edge sensitivity. The experimental setup is shown in Figure 6.5 The signal of the sensor pair triggered a CMS reference telescope made of silicon microstrip detector modules. The gap width between the edgeless sensors was determined using the tracks of the reference telescope, and was then compared with the above results of precision metrology.

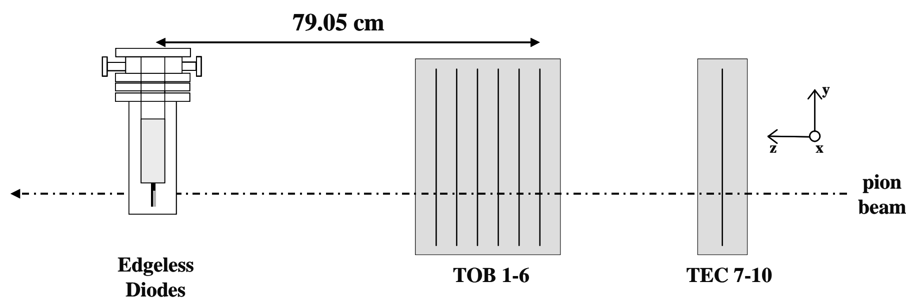

Figure 6.5 Layout of the test beam setup at the X5 west experimental area at CERN.

The CMS telescope consisted of 6 silicon detector modules with vertical strips of 183 µm pitch (TOBs[1] 1 to 6) and one plane with 4 wedge-shaped modules (TECs[2]) organized in a petal configuration with strip pitches varying between 166 µm and 207 µm along the strips. The beam traversed the petals in an area with nearly horizontal strips, yielding the vertical distribution of the beam. The beam distribution along this coordinate is only used for determining the average gap width and can be estimated assuming that the petal detectors are perfect rectangles with strips of 200 µm pitch.

1 CMS Tracker Outer Barrel modules.
2 CMS Tracker Endcap modules.

Figure 6.6 The CMS tracker used as a reference telescope triggered by the pair of edgeless diodes, which consists of six planes with vertical microstrip silicon detector modules (TOBs) cooled to -20 °C.

Unfortunately, after a power cut during the beam tests, one of the modules with vertical microstrip detectors was damaged, and therefore only five planes could be used. The positions along the beam axis of the five working TOBs were 0.0, 5.04, 10.08, 15.12 and 25.20 cm. Our pair of edgeless diodes were 79.5 cm away from the TOB 1.

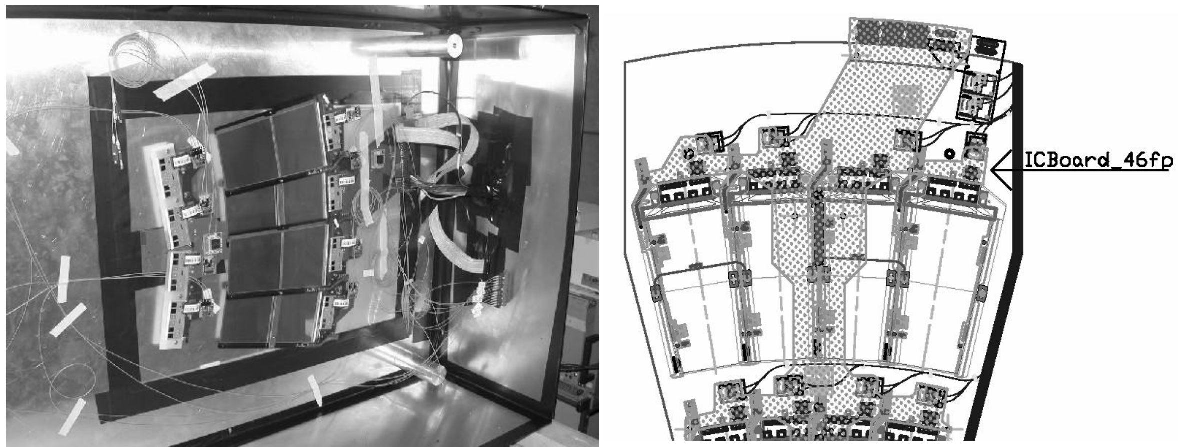

Figure 6.7 The CMS tracker used as a reference telescope triggered by the pair of edgeless diodes, had four horizontal planes arranged in a petal configuration (TECs).

The pair of edgeless diodes was mounted on a printed circuit board (PCB) holder in a small cryostat as shown by Figure 6.4 The aluminum vacuum vessel of 90 mm diameter has a 500 μm thick window to minimize multiple scattering. The inner vessel holds liquid N_2, which cools the PCB holder by conduction. A top flange connects the two vessels mechanically, and provides ports for the vacuum pumping line and for a hermetic feed-through for the detector and instrumentation connections. A thin

copper shield surrounds the PCBs so as to reduce thermal radiation. The PCB is mounted on a motherboard, which is connected to the liquid nitrogen bath via a thermal bridge. A heater and a thermometer on the sensor holder PCB enable precise control of its temperature between 90 K and 200 K. The setup can hold a ^{90}Sr source, which was used for characterization of the diodes in the laboratory [52]. Leak tests were carried out with a two stage PT50 vacuum pump and a vacuum of 2.4 10^{-4} mbar was achieved. The electrical feed-throughs leaked at a rate of 10^{-7} mbar l/s, which is acceptable for the required vacuum.

X5 Beam

The X5 beam is a secondary or tertiary particle beam that provides hadrons, electrons or muons of energies between 5 and 250 GeV [53]. This beam is part of the West Area test beam complex at CERN, which is derived from the H3 secondary beam (see Figure 6.8).

A 400 GeV/c primary proton beam is extracted from the SPS and directed towards the T1 primary target. The typical intensity of this primary beam is 2 10^{12} protons per burst. From the T1 target a secondary beam is derived, called the H3 beam, with 120 GeV/c (top momentum 250 GeV/c) particles, mainly pions and electrons.

The H3 beam is split into two branches, each of which transports up to about 1.5 10^{7} particles to the X5 and X7 secondary targets. At X5, the spot size is of the order of a few millimetres RMS in each projection. Both the X5 and X7 beams provide the zones downstream of them with muons.

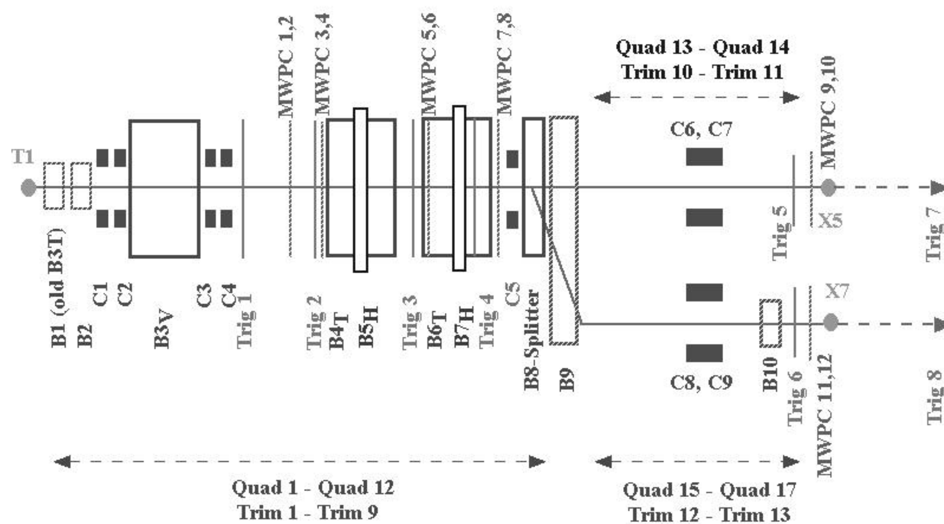

Figure 6.8 Schematic layout of the H3/X5 beam.

The beam can be operated in three rather different ways, namely as a secondary beam, as a versatile tertiary beam or as a muon beam. For secondary beam operation the empty target head is selected and the X5 beam is tuned to the same momentum as the H3 parent beam. The maximum allowed intensity in this mode is 10^{6} particles per SPS cycle. In tertiary mode the target head defines the particle type. Three different target heads are available, namely lead (4 mm), copper (400 mm) or beryllium

(400 mm). Pion beams are obtained using the copper target. We were working most of the time with a tertiary beam with pions.

6.4 Analysis of the data

Data were taken with the CMS reference tracker using the edgeless diode pair as a trigger. Three main runs, where the edgeless diodes were biased to 50 V, 100 V and 150 V, have been fully analysed.

The impact coordinates of the reference tracker planes were extracted using the ORCA[1] CMS software [54]. In absence of magnetic field the tracks can be fitted with straight lines, and extrapolated to the plane of the edgeless diodes. As the vertical y coordinate of the tracks was determined in one plane, only the projection of the tracks onto an horizontal plane could be determined. To determine the insensitive area of the edgeless diodes, the average effective gap width measured with the beam was then compared with the direct measurements on the metrology table.

Track fits. Least squares estimates of the fit parameters

In the absence of magnetic field, the x-coordinate of the impact points at the five vertical strip detectors should lie on a straight line, which can be fitted with the analytical expression

$$x = a \cdot z + b \tag{6.4}$$

where the slope a and the intercept b are the free parameters of the fit. The z-axis is defined along the beam direction and the x-axis along the horizontal component perpendicular both to the beam and to the strips. The parameters a and b as well as their standard deviations σ_a and σ_b and covariance cov(a,b) are given by the linear regression fit [55]. Figure 6.9 and Figure 6.10 show a typical distribution of these parameters for a run triggered with scintillators. Tracking was done only when all the planes were fired and only one cluster (combination of hits on consecutive strips) was found at each plane.

A priori, a single distribution for a would have been expected, since it describes the horizontal angular distribution of the beam. However, two well differentiated distributions are observed. From the beam optics, this might be due to the decay of relativistic pions into a muon and a neutrino[2]. Therefore, what is observed in the figure is the momentum difference between pions and muons. The relative intensities seem not to agree with this explanation, since the pion peak should be considerably much larger than the muon one. A simple explanation for that is the fact that the plotted data corresponds to mixed runs, some of which are with a 100 % muon beam. This would account for the small intensity difference.

1 Object Oriented Reconstruction for CMS Analysis. ORCA 7.1.0, User Guide, 2003.
2 Private communication with L. Gatignon.

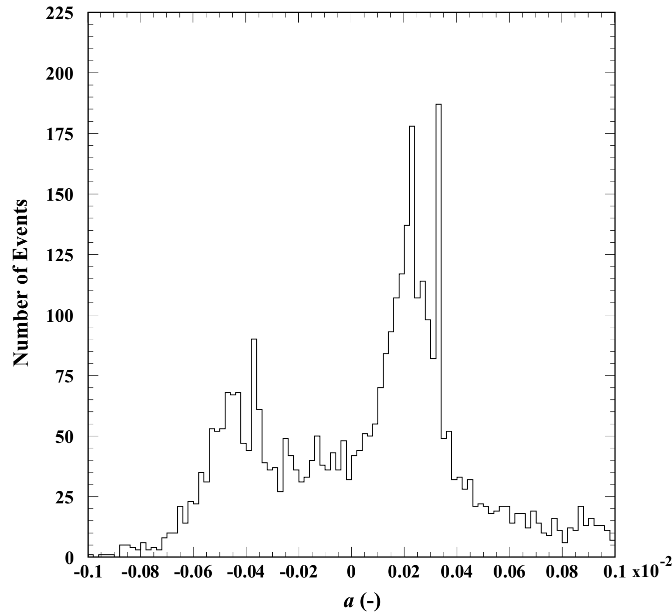

Figure 6.9 Distribution of the parameter *a* of the fitted tracks for a CMS run triggered with scintillators (4261 entries) where two overlapping distributions can be observed: the right peak is due to pions, and the left peak plus the broad distribution are mainly due to muons.

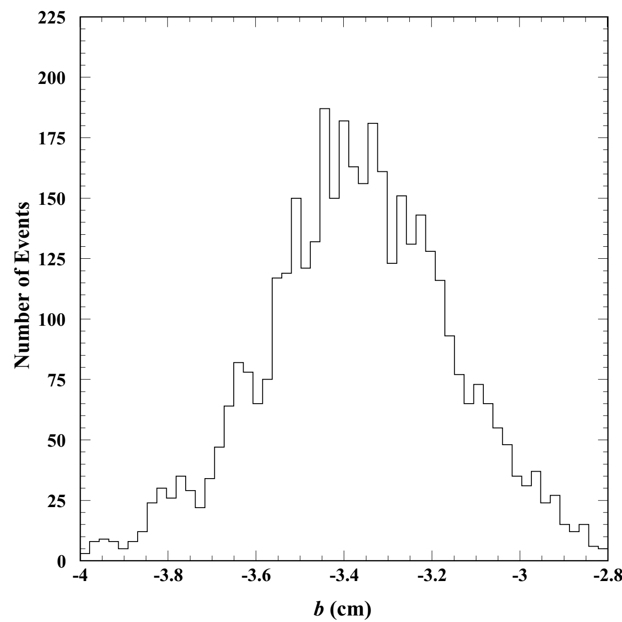

Figure 6.10 Distribution of the parameter *b* of the fitted tracks for a CMS run triggered with scintillators, where the effect of some dead strips on the reference tracker can be observed on the left part of the histogram.

After calculating *a* and *b* for each track triggered by the edgeless diode pair, the extrapolation of the track to the plane of the diodes (x_d, z_d), and the standard deviation of the impact point (σ_{xd}), can be calculated by:

$$x_{\mathrm{d}} = a \cdot z_{\mathrm{d}} + b \tag{6.5}$$

$$\sigma_{x\mathrm{d}}{}^2 = \sigma_b{}^2 + z_{\mathrm{d}}^2 \cdot \sigma_a{}^2 + 2 \cdot z_{\mathrm{d}} \cdot \mathrm{cov}(a, b)\,. \tag{6.6}$$

The least squares estimates of parameters *a* and *b* are [55][56][57]:

$$a = \frac{N \cdot \sum_{i=1}^{N} x_i \cdot z_i - \sum_{i=1}^{N} z_i \cdot \sum_{i=1}^{N} x_i}{N \cdot \sum_{i=1}^{N} z_i^2 - \left(\sum_{i=1}^{N} z_i\right)^2}\,, \tag{6.7}$$

$$b = \bar{x} - a \cdot \bar{z}\,, \tag{6.8}$$

where

$$\bar{x} = \frac{1}{N}\sum_{i=1}^{N} x_i \qquad \bar{z} = \frac{1}{N}\sum_{i=1}^{N} z_i\,, \tag{6.9}$$

and *N* is the number of points to fit. The squared errors are:

$$\sigma_a^2 = \frac{\sigma_x^2}{\sum_{i=1}^{N} z_i^2 - \frac{1}{N}\left(\sum_{i=1}^{N} z_i\right)^2}\,, \tag{6.10}$$

$$\sigma_b^2 = \frac{\sum_{i=1}^{N} z_i^2}{N}\sigma_a^2\,, \tag{6.11}$$

where $\sigma_x{}^2$ can be estimated as:

$$\sigma_x^2 = max\{\sqrt{\frac{\varepsilon(a, b)}{N-2}}, \Delta x\}\,, \tag{6.12}$$

where σ_x is the error of the impact point at each tracker plane, $\varepsilon(a,b)$ is the sum of the squares of the residuals at each of the *N* planes, and Δx is the theoretical estimate for the tracking precision for a single plane, to be discussed below. The covariance between the two parameters *a* and *b* (last term in Equation 6.6), can also be derived from the least squares theory:

$$\mathrm{cov}(a, b) = -\frac{\sum_{i=1}^{N} z_i}{N}\,\sigma_a^2. \tag{6.13}$$

The covariance accounts for the correlation of *a* and *b* and should not be neglected, since this could lead to an overestimate for the error.

The standard deviation σ_{xd} estimates the smearing of the beam image of the sharp edges of the sensor due to the tracker resolution. The comparison of this magnitude with the effective smearing σ_g, determined from the data, indicates how well the performance of the tracker is understood, if the effective edges of the gap are sharp.

On the other hand, if the efficiency of the edge region exhibits a gradual reduction towards the physical edge with gaussian shape characterized by the width of the efficiency loss σ_{el}, this smearing should add with the smearing due to the tracker resolution. Moreover, if the edges are not perfectly straight, with gaussian deviations characterized by the distribution width σ_e, the smearing of the effective gap edge becomes:

$$\sigma_g^2 = \sigma_{xd}^2 + \sigma_{el}^2 + \sigma_e^2 \tag{6.14}$$

However, if the efficiency is reduced only in a region much smaller than σ_{xd}, and the edges deviate from straight lines much less than σ_{xd}, the root of the square sum will not deviate substantially from σ_{xd} itself, and therefore the sum $\sigma_{el}^2 + \sigma_e^2$ cannot be accurately determined from the difference $\sigma_g^2 - \sigma_{xd}^2$. The effective gap width will in such a case remain the best estimator for the possible loss of efficiency near the edges.

The track resolution at the trigger diodes, i.e. the standard deviation σ_{xd} of the impact point at z_d, can be determined in two ways: using the tracker geometry and data alone. The first is based on the theoretical position resolution of the microstrip detectors, calculable from the strip pitch p = 183 µm of the sensor and from the noise performance of the analog signal readout, if the charge is shared between two or more strips. The second is based on the estimation of the position resolution of the microstrip detector, as discussed above, from the distribution of the residuals in a set of fitted tracks, such as that used for the alignment of the tracker detectors.

Knowing the distance z_d = 79.05 cm and the geometry of the tracker planes, and estimating the error in the *x* coordinate in a conservative way as for a digital microstrip sensor by the standard deviation of a uniform distribution of width *p*:

$$\Delta x = \frac{p}{\sqrt{12}} \approx 53\mu m \tag{6.15}$$

we can obtain a conservative approximation of the error in the *x* extrapolated to the diode plane, which comes out to be 186 µm. The intermediate results of this calculation are collected in Table 6.1:

Table 6.1 Errors for *a*, *b* and cov(*a*,*b*)

σ_a (-)	$2.72\ 10^{-4}$
σ_b (cm)	$3.83\ 10^{-3}$
cov(*a*,*b*) (cm)	$-\ 8.23\ 10^{-7}$

The residuals (difference between impact point and the value calculated with the fit track) at each plane are in fair agreement with the 53 µm resolution calculated above for a digital sensor as shown by Figure 6.11. Values somewhat smaller than this are found for each tracker plane, since we are using APV25 analog readout chips and the charge sharing between neighboring strips is taken into account in

a fraction of track hits. However, they are not far from the conservative value since the strips are rather wide (183 μm) and therefore a high percentage of the clusters do not show charge sharing between multiple strips. As shown by Figure 6.12, in about 70 % of the cases only one strip is hit and in 20 % of the cases the clusers present charge sharing between 2 strips.

Peaks probably due to noisy strips can be observed in the residual plots Figure 6.11. The alignment was done with respect to the TOB 1 using the data from four runs. The offsets applied for correction of the misalignment of the centers of the sensors were the following:

Table 6.2 Offset applied to the tracker planes to align their centers respect to the TOB 1.

MODULE	z_i **(cm)**	**offset / pitch**	**Offset (μm)**
1 TOB	0.0	0.0	0.0
2 TOB	5.04	-3.435	628.6
3 TOB	10.08	0.931	170.4
4 TOB	15.12	0.78	142.7
5 TOB	25.20	8.34	1526.2

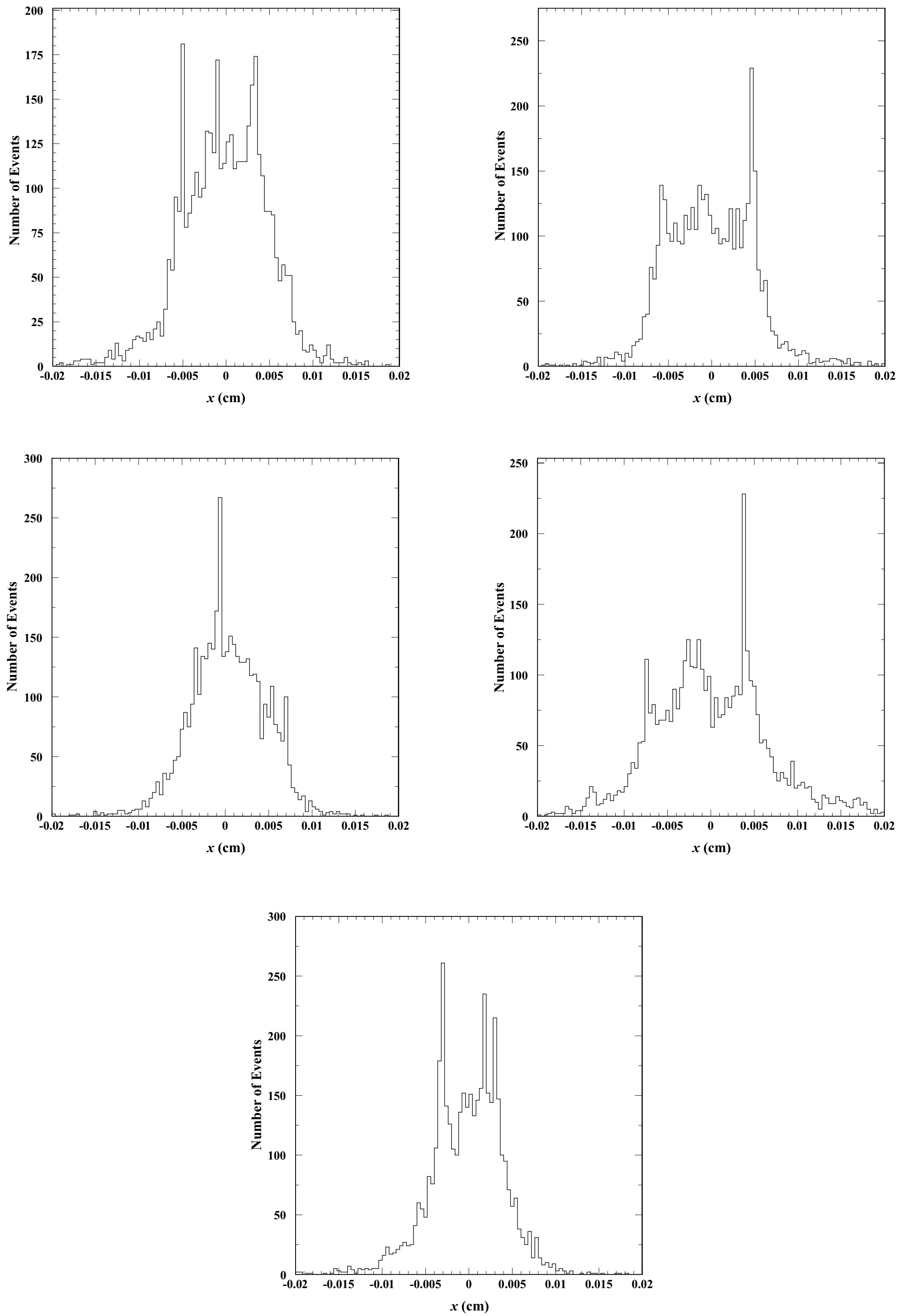

Figure 6.11 Residuals at tracker TOBs 1,2,3,4 and 5 (from left to right and from top to bottom).

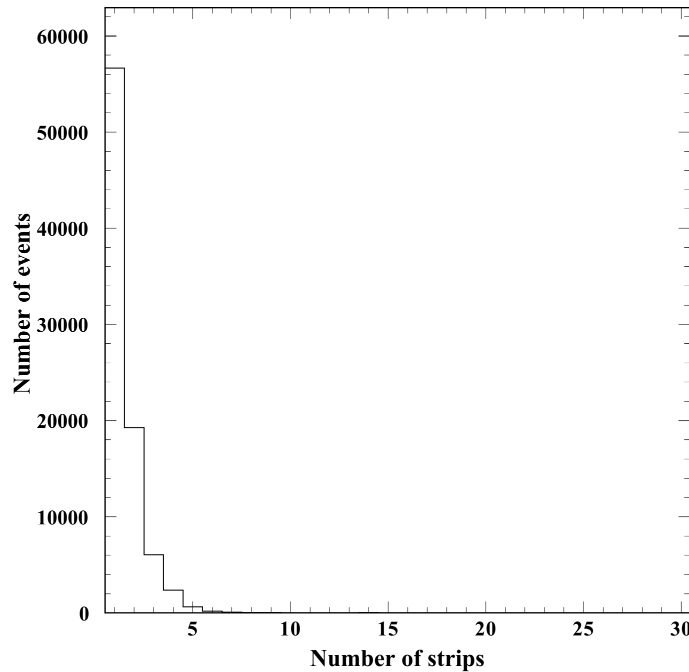

Figure 6.12 Number of strips for each cluster.

The distributions of σ_a and σ_b (Figure 6.13) show tails which are probably due to noise or parasitics, which increase the mean values of these errors. Their most probable values are therefore better estimates to be used for the error in the extrapolation of the tracks. Inserting the most probable values of the distributions of σ_a and σ_b in Equation 6.6 then yields

$$\sigma_{xd} = 170\mu m\,. \tag{6.16}$$

.

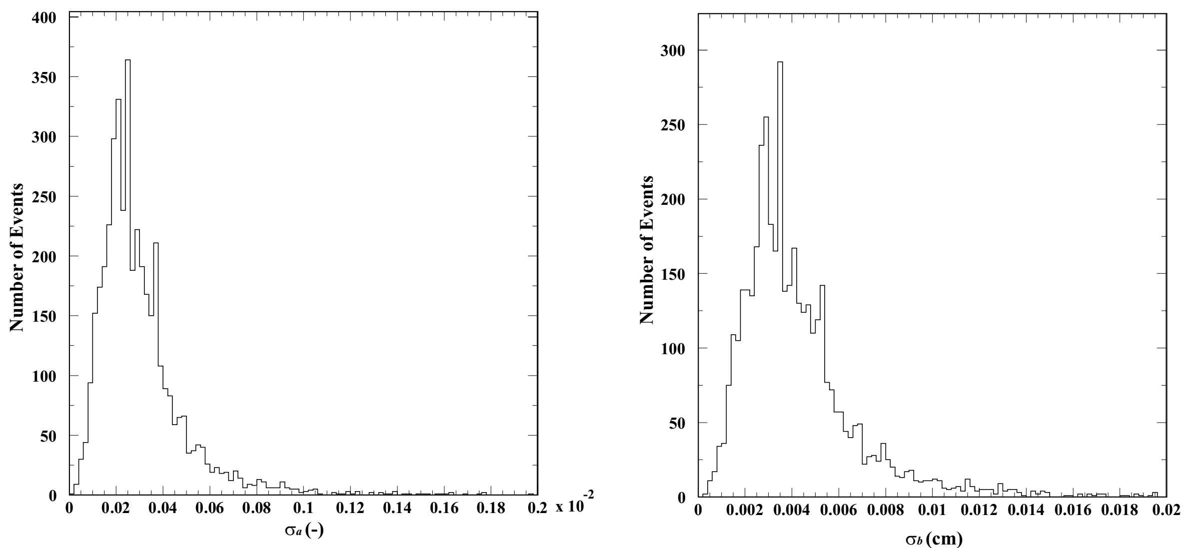

Figure 6.13 Distribution of σ_a and σ_b calculated for each track.

Several assumptions must be made to be able to extract the effective width of the gap from its beam image. A simple Monte Carlo simulation was therefore made to estimate the possible systematic errors resulting from the neglect of the beam intensity variation within the effective gap. A beam with gaussian width $\sigma = 0.19$ cm was simulated using the *rnorml(,)* function from the CERN Program Library. A 450 µm gap between the pair of edgeless diodes was modeled as a step function and the impact points scattered using an independent gaussian with a $\sigma = 186$ µm simulating the tracker resolution. The resulting simulated images of the pair of diodes with infinite and finite tracker resolutions are plotted in Figure 6.14 (scatter plot) and Figure 6.15 (projection onto x-axis).

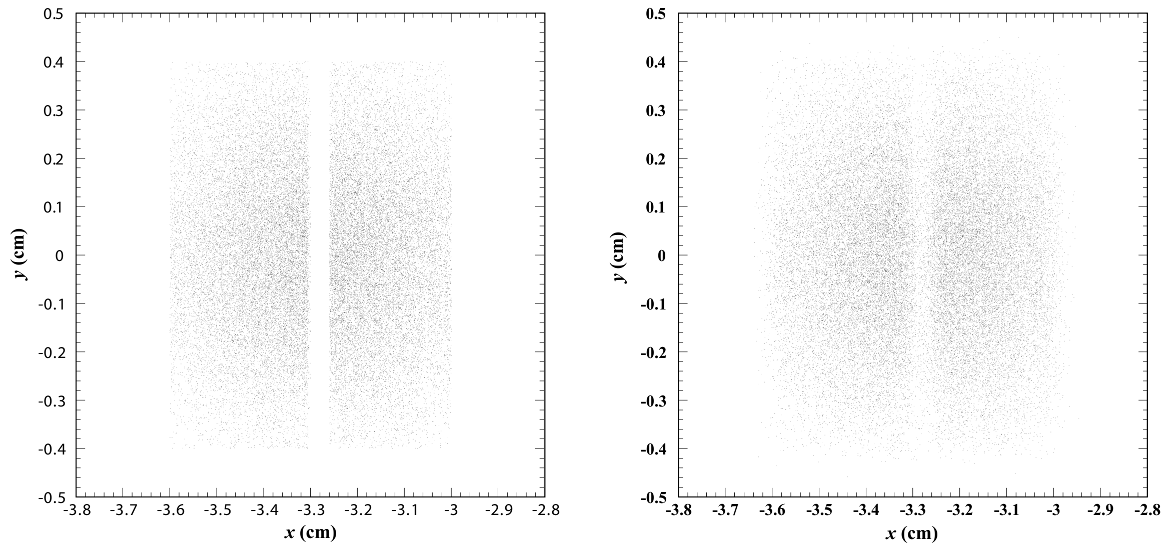

Figure 6.14 Simulated 2D image of the pair of edgeless diodes with a constant gap of 450 µm given by a tracker with infinite resolution (left) and finite resolution of 186 µm (right).

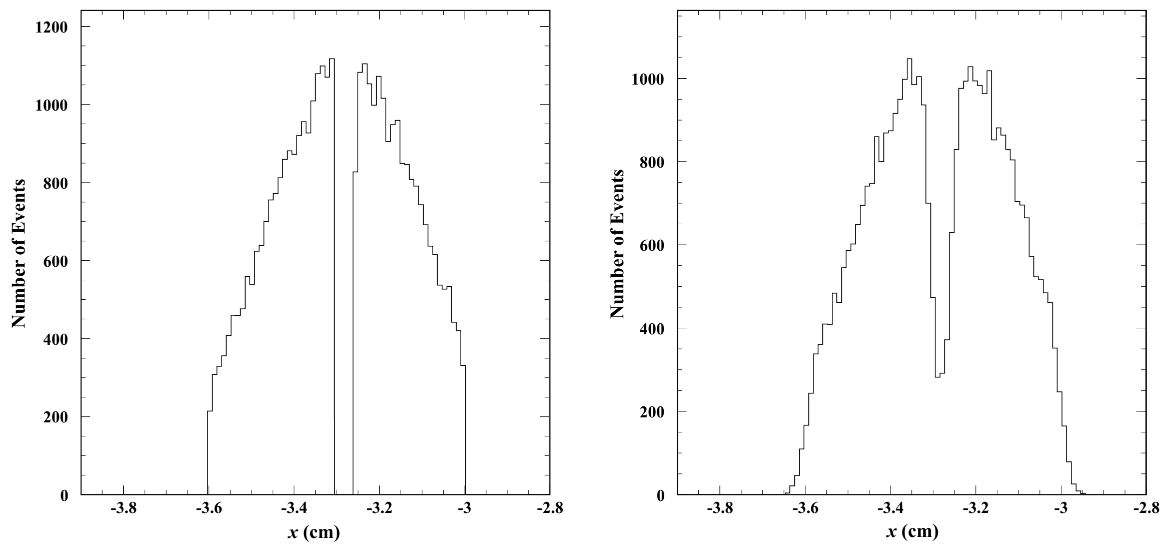

Figure 6.15 Simulated 1D image of the pair of edgeless diodes with a constant gap of 450 µm given by a tracker with infinite resolution (left) and finite resolution of 186 µm (right).

Model function for the beam image of the gap

The model function $N(x)$ that we shall use to describe the beam image of the gap can be expressed in terms of three distribution functions $B(x)$, $G(x)$ and $H(x)$, which shall describe, respectively, the beam shape, the gap width and the tracker resolution.

The beam shape was studied using a CMS run (not triggered by the pair of edgeless diodes but scintillators). Several functions were used to fit the beam shape, namely a gaussian, a polynomial convoluted to a gaussian and a double exponential function. However, no significant difference between the fits with the three functions was observed and therefore a gaussian function $B(x)$ was chosen to describe the beam.

$$B(x) = C\exp\left(\frac{-(x-\mu_B)^2}{2\sigma_B^2}\right). \tag{6.17}$$

Fits with χ^2/nfd between 2.2 and 4.7 are obtained when the beam profile at each tracker plane is fitted with a gaussian function. Figure 6.16 shows the result of a gaussian fit for the first TOB.

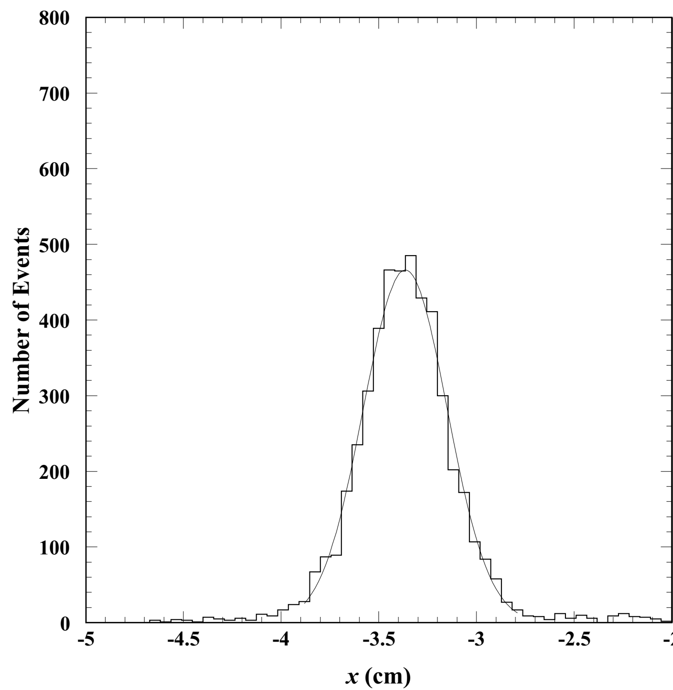

Figure 6.16 TOB 1 image of the beam and fit with a gaussian function.

The borders of the pair of edgeless diodes is described with the sum $G(x)$ of two step functions, because the tracker resolution is quite poor and unlikely to enable the extraction of the edge resolution of the detectors themselves. The tracking resolution is described with a gaussian function $H(x)$.

If the tracker had infinite resolution, i.e. $H(x) = \delta(x)$ the number of counts $N(x)$ in our histogram would be

$$N(x) = B(x) \cdot G(x) \cdot dx \tag{6.18}$$

In order to describe the smearing of the effective gap due to the limited tracker resolution, one has to convolute Equation 6.18 and $H(x)$:

$$N(x) = \int_{-\infty}^{\infty} B(x') \cdot G(x') \cdot H(x-x')dx' \quad (6.19)$$

Assuming that $B(x)$ is constant in the area where the smearing takes place, the integration can be performed analytically:

$$N(x) = B(x)\int_{-\infty}^{\infty} G(x') \cdot H(x-x')dx' \quad (6.20)$$

$$N(x) = B(x)\int_{-\infty}^{\infty} G(x') \cdot \frac{1}{\sigma_g\sqrt{2\pi}}\exp\left(\frac{-(x-x')^2}{2 \cdot \sigma_g^{\ 2}}\right)dx' \quad (6.21)$$

$$N(x) = B(x)\left(\int_{-\infty}^{\mu_g - \frac{d_g}{2}} \frac{1}{\sigma_g\sqrt{2\pi}}\exp\left(\frac{-(x-x')^2}{2 \cdot \sigma_g^{\ 2}}\right)dx' + \int_{\mu_g + \frac{d_g}{2}}^{\infty} \frac{1}{\sigma_g\sqrt{2\pi}}\exp\left(\frac{-(x-x')^2}{2 \cdot \sigma_g^{\ 2}}\right)dx'\right) \quad (6.22)$$

where d_g is the gap width and μ_g the gap center. The complementary error function being:

$$\text{erfc}(x) = \frac{2}{\sqrt{\pi}}\int_x^{\infty} e^{-t^2}dt \quad (6.23)$$

the gap smearing function can be expressed in terms of complementary error functions. If the beam is considered to be gaussian, then:

$$N(x) = \frac{1}{\sigma_B\sqrt{2\pi}}\exp\left(\frac{-(x-\mu_B)^2}{2 \cdot \sigma_B^{\ 2}}\right)\left(\frac{1}{2}\text{erfc}\left(\frac{x-\mu_g+\frac{d_g}{2}}{\sqrt{2} \cdot \sigma_g}\right) + \frac{1}{2}\text{erfc}\left(\frac{x-\mu_g-\frac{d_g}{2}}{\sqrt{2} \cdot \sigma_g}\right)\right) \quad (6.24)$$

where the change of variable used is:

$$t = \frac{x-x'}{\sqrt{2}\sigma_g} \quad (6.25)$$

The gap smearing function can then be expressed in terms of complementary error functions, and if the beam is gaussian, the experimental spectrum can then be approximated by

$$N(x) = \text{B}\exp\left(\frac{-(x-\mu_B)^2}{2 \cdot \sigma_B^{\ 2}}\right)\left(\text{erfc}\left(\frac{x-\mu_g+\frac{d_g}{2}}{\sqrt{2} \cdot \sigma_g}\right) + \text{erfc}\left(\frac{x-\mu_g-\frac{d_g}{2}}{\sqrt{2} \cdot \sigma_g}\right)\right) \quad (6.26)$$

where B is a beam normalization constant, μ_B is the center of the beam, σ_B is the width of the beam, d_g is the gap width between the edgeless sides of the sensors, σ_g is the effective edge resolution, and μ_g is

the center of the gap. Equation 6.26 will be referred to as *model function for the track distribution*, or *model function* in short.

Results of the fits

The values of the fit parameters are those obtained by minimizing the χ^2 of the fit of the model function for the track distribution to the histogram of the number of tracks as a function of x_d. The minimization was performed using the MINUIT package [58]. The results of the three main runs are presented below in Table 6.3. Only tracks with impact at the five planes have been considered, and tracks with planes having several clusters have been rejected.

Table 6.3 Results of the fits for the three runs at different bias potentials (statistical error only).

Parameter	**Symbol**	**Units**	**U_{bias}= 50 V**	**U_{bias}= 100 V**	**U_{bias}= 150 V**
Number of tracks			30659	491861	226486
Beam normalization	B		1334 ± 13	23360 ± 63	10284 ± 42
Beam center	μ_B	cm	-3.201 ± 0.013	-3.373 ± 0.001	-3.334 ± 0.001
Beam width	σ_B	cm	0.299 ± 0.086	0.190 ± 0.001	0.190 ± 0.001
Gap width	d_g	µm	435 ± 14	463 ± 3	389 ± 5
Effective edge resolution	σ_g	µm	180 ± 7	180 ± 2	162 ± 3
Gap center	μ_g	cm	-3.335 ± 0.006	-3.325 ± 0.001	-3.316 ± 0.001

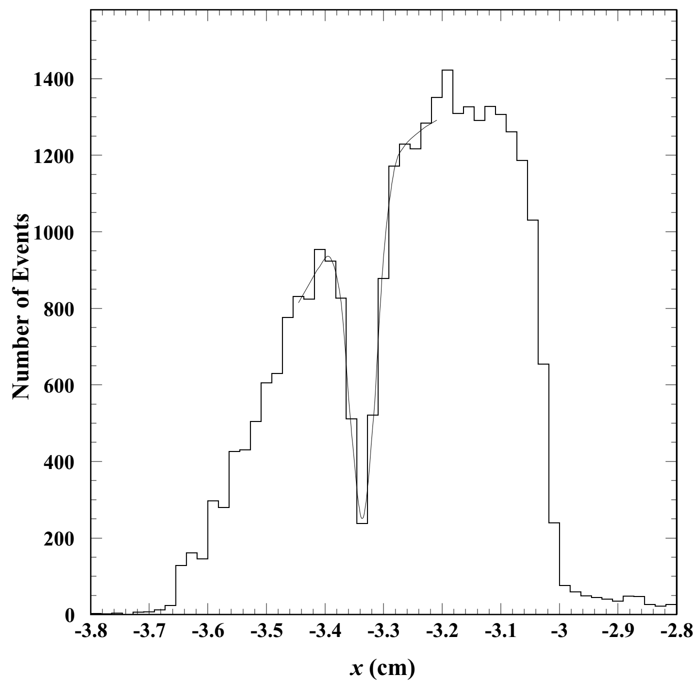

Figure 6.17 The x-distribution of the extrapolated tracks at the edgeless pair of cut diodes plane biased at a potential of 50 V.

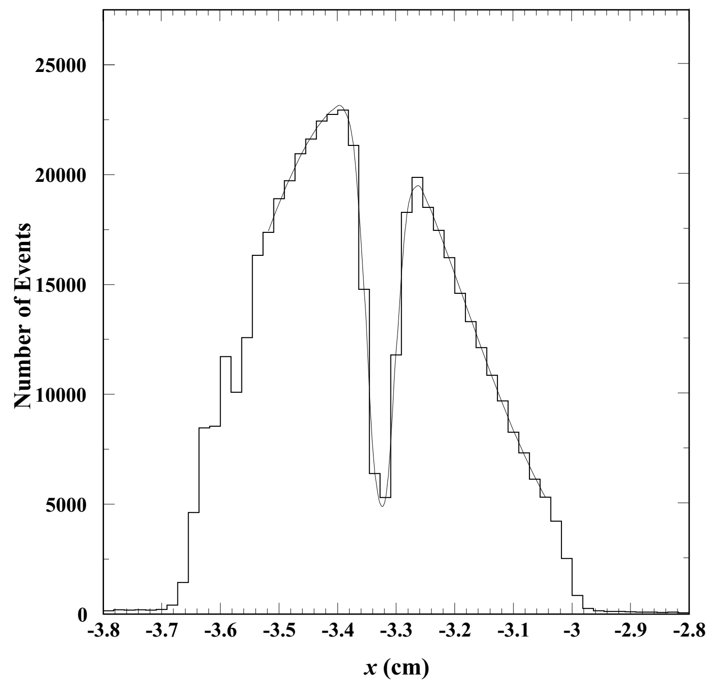

Figure 6.18 The x-distribution of the extrapolated tracks at the edgeless pair of cut diodes plane biased at a potential of 100 V.

For this set of runs the impact points as given by the ORCA reconstruction software at each CMS tracker plane are presented as well (Figure 6.19). The improvement of resolution for the planes which are located closer to the diode can be observed. There is less smearing at the diode edge for TOB 5, closer to the diode, than for TOB 1. Several dead strips at plane 4 and the smearing of these strips when tracking at different planes can be also seen.

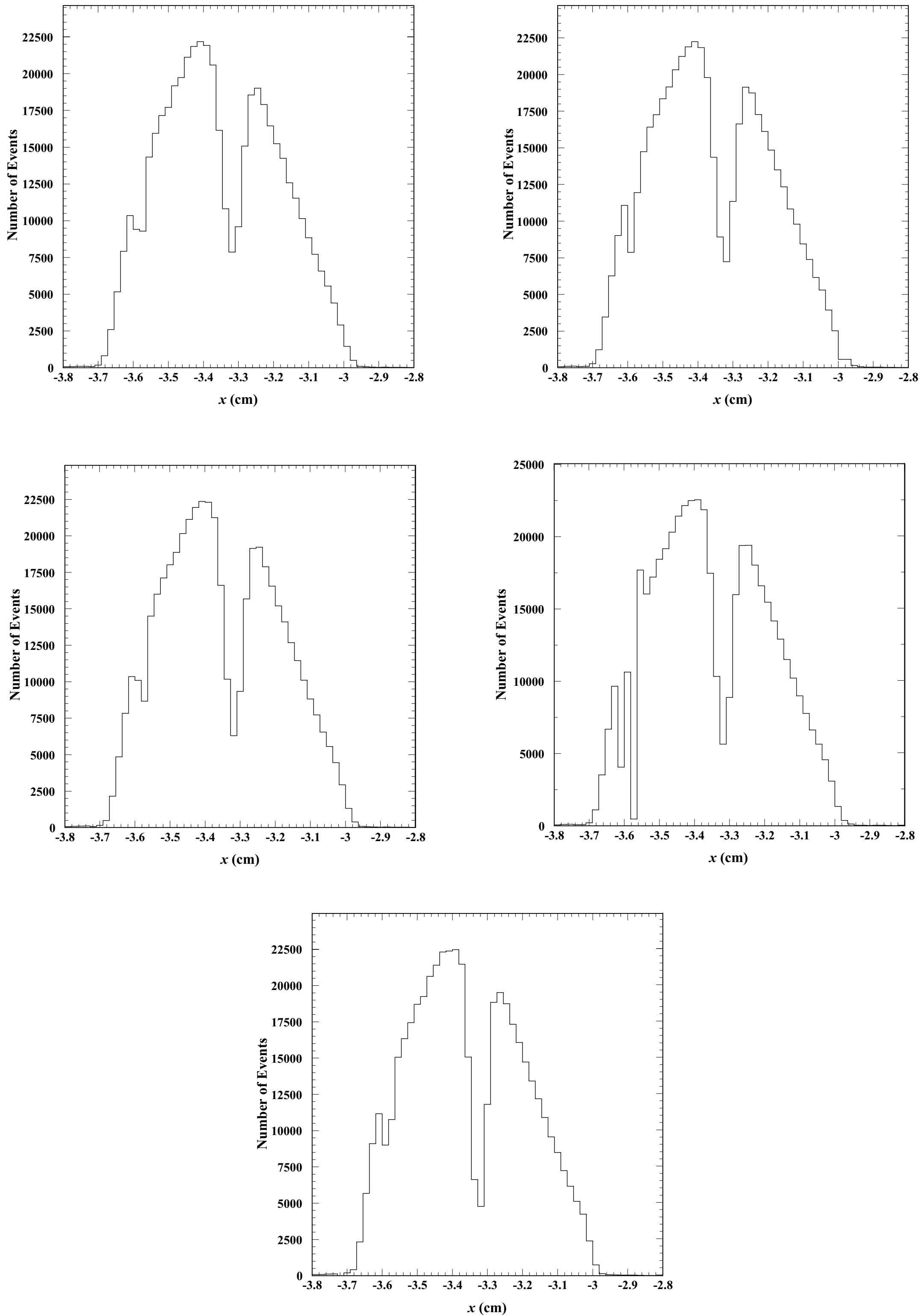

Figure 6.19 Impact coordinates at planes 1, 2, 3, 4 and 5 of the reference tracker when triggering with the pair of edgeless diodes biased at a potential of 100 V.

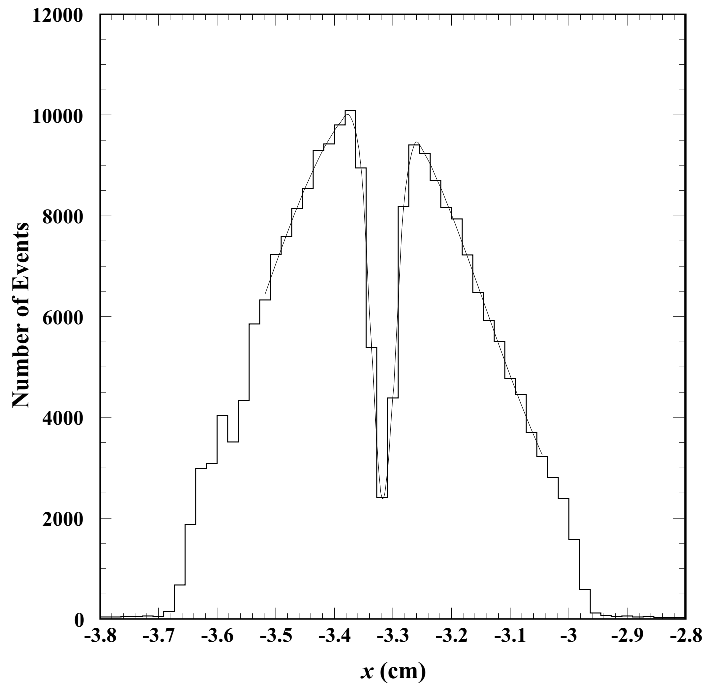

Figure 6.20 The x-distribution of the extrapolated tracks at the edgeless pair of cut diodes plane biased at a potential of 150 V.

6.5 Errors in determining the gap width between diodes

The gap width was measured by an optical probe on a metrology table, as described before. The effective width of the gap, where the dead layers may contribute, was determined by the fitting method described above, using the tracker data selected by our trigger. These two measurements are then subtracted to determine the depth of the insensitive layer at the edges of the sensors, which turns out to be very small. It is therefore necessary to examine carefully the various sources of error, in order to improve the confidence in the result that is close to zero.

Effective gap measured with the beam

There are statistical errors coming from the fit of the results using the model function, and systematic errors in the function itself. Their combination yields the final accuracy of the effective gap width determined by the beam.

The statistical error in the estimation of the effective dead gap size is given by the MINUIT error estimate of the fit of the parameter d_g. The fit results in Table 6.3 yield statistical errors from 3 µm to 14 µm. As expected, this error is larger for the 50 V bias run, with only 3 10^4 events than for the 100 V bias run, which counts with half a million tracks.

Our model function has three main systematic uncertainties. A first systematic error is due to the consideration of the beam shape as constant close to the gap center, for mathematical simplification. This error has been estimated using the MC simulation by comparing the modeled and fitted gap width

parameter. The difference between these values is 5 µm, which has been taken as an estimate for the magnitude of this systematic error.

A second source of systematic error is the approximate character of the fitted functions, mainly because the beam is not be perfectly gaussian. The error due to this assumption was estimated by observing the change of the gap width parameter d_g when varying the number of bins of the data and therefore the region in which the fit is performed. By applying such a procedure for the three main runs (Figure 6.17, 6.18 and 6.20), this error comes out to be of the order of 4 µm. As shown in the Figure 6.21, for the highest statistics run a *plateau* is found between 18 and 27 bins, where the gap width parameter remains nearly constant and the χ^2 is close to 1. Therefore, the chosen parameter values for each run (Table 6.3) correspond to fits with 25 bins (a large number of bins within the *plateau*).

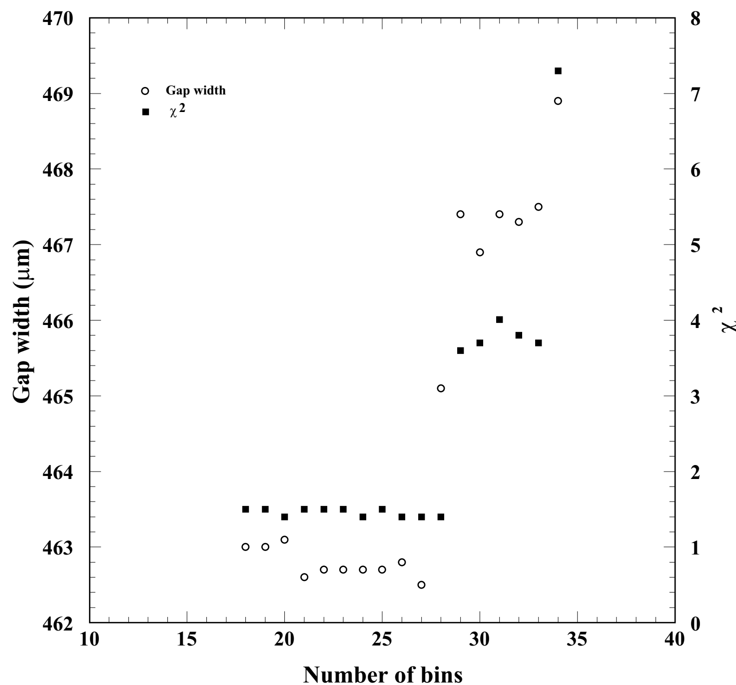

Figure 6.21 Gap width parameter and χ^2 as a function of the number of bins included in the fit, for the 100 V bias potential run.

A third source of error comes from the fact that the tracker resolution may not be gaussian, since the strips of the telescope detectors are pretty wide, and behave as in a digital sensor. This error can be evaluated with the error found in the fits for the effective edge resolution, and ranges from 2 µm to 7 µm, as shown in Table 6.3. The effective edge resolution obtained with the fit and the tracker fit data alone are in good agreement. The largest effective edge resolution is found for the longest run, which can be understood if we consider that the mechanical stability of the cryostat support was far from the 10 µm level which would be desirable. The mechanical instability of the support may cause a drift of the position of the gap, leading to additional smearing that adds to the tracker resolution. The correlation between the d_g and σ_g parameters was also studied and proved not to be correlated (Figure 6.22).

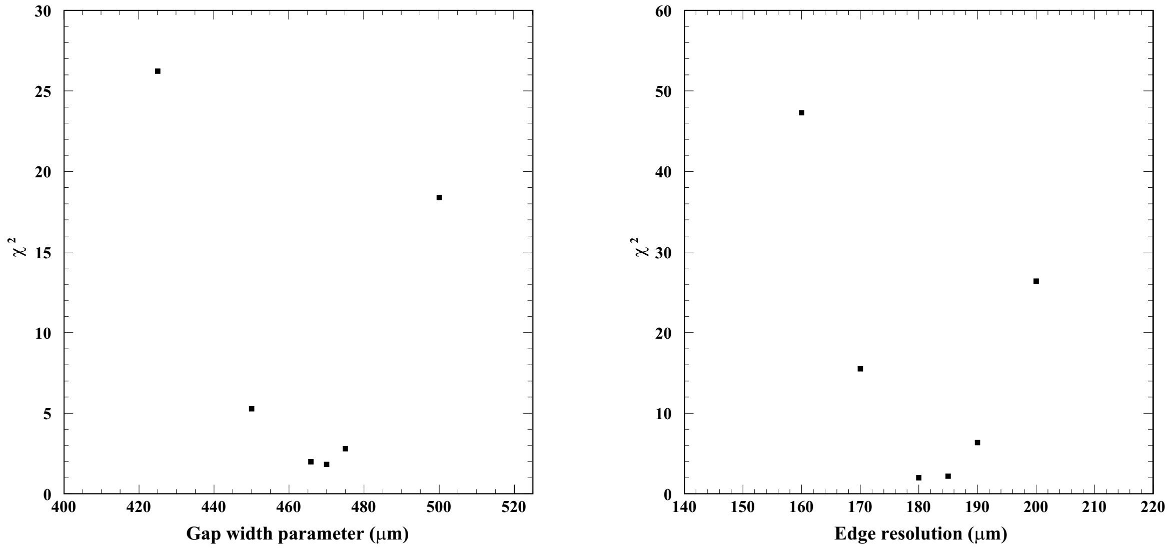

Figure 6.22 Left: variation of the χ^2 of the fit with d_g when σ_g is fixed to 180 μm. Right: variation of the χ^2 of the fit with σ_g when d_g is fixed to 470 μm.

The statistical and systematic sources of error are summarized in Table 6.4. The three systematic errors are uncorrelated, and are therefore added linearly.

Table 6.4 Statistical and systematic errors of the effective gap width.

Error source	**Units**	**U_{bias}= 50 V**	**U_{bias}= 100 V**	**U_{bias}= 150 V**
Fit (stat.)	μm	14	3	5
Non-gaussian beam (syst.)	μm	4	4	4
Non-gaussian tracker resolution (syst.)	μm	7	2	3
No convolution of the beam (syst.)	μm	5	5	5
Lin. sum of systematic errors	μm	16	11	12

Gap measurement on a metrology table

The gap measurement on the metrology table has a measurement error, which is the accuracy of the metrology measurement itself (±3 μm), and there is as well an error due to minor chipping at the edge and to slight non-parallelism of the edges, as the gap is not constant from top to bottom.

Figure 6.23 shows that the beam profile along the vertical coordinate is rather flat at the diode region. The average width of the gap, weighted by the relative beam intensity [59] is ($418 \pm 11_{stat.}$) μm. These errors and the root of their square sum are summarized in Table 6.5.

Table 6.5 Errors in the measurement of the gap on the metrology table.

Error source	**Units**	**Error**
Gap width variation	μm	11
Accuracy of the metrology	μm	3
Sum (stat.)	μm	11

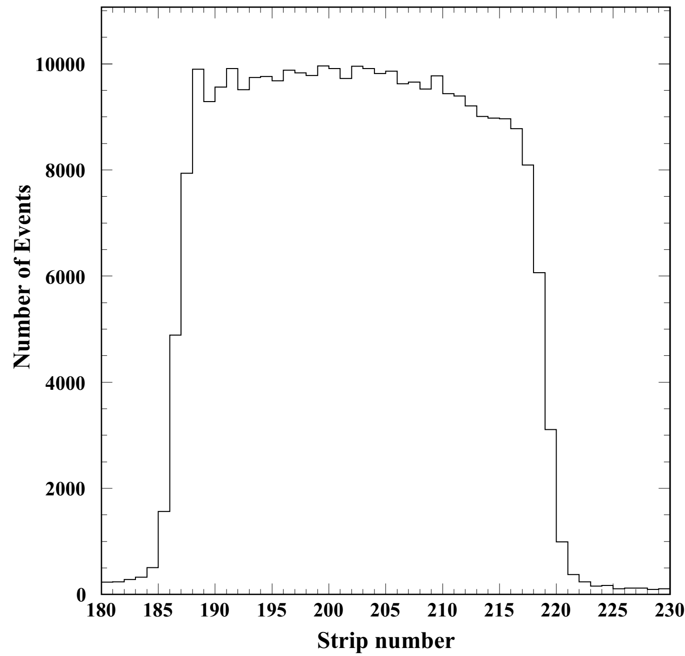

Figure 6.23 Distribution of the hit strips from one of the petal CMS sensors with horizontal strips.

All the results are shown in Figure 6.24:

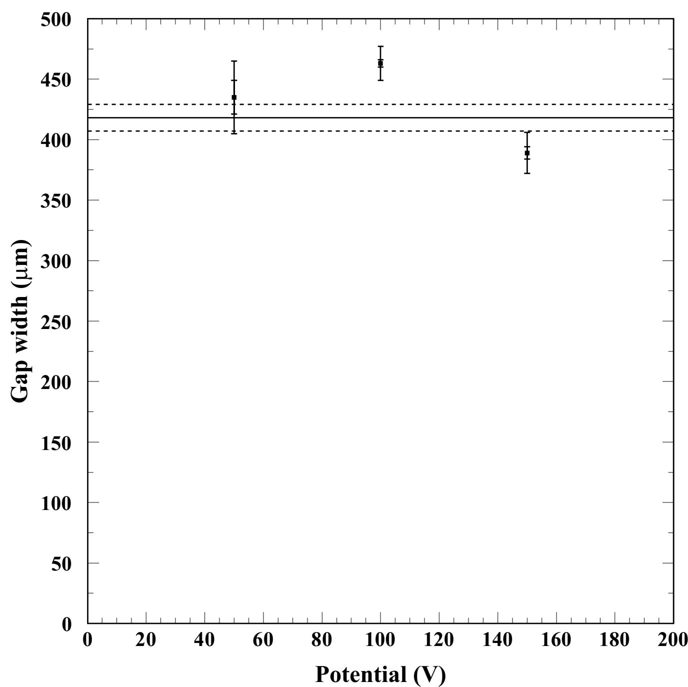

Figure 6.24 Comparison between metrology and beam measurements of the gap width between the pair of edgeless diodes. The horizontal line shows the optically measured average gap width, with its statistical error limits shown by dashed lines. The data points refer to beam measurements at different bias potentials. The smaller bars on data points show their statistical errors, and the larger ones the sum of the statistical and systematic errors.

6.6 Insensitive area of the edgeless diode

The effective gap measured by the beam on one hand, and the gap measured on the metrology table on the other, can now be compared, in order to estimate the size of the insensitive layer of silicon at the edges of the devices.

There is no evidence of systematic dependence of the gap width with the bias potential, which seems logical since the diode is fully depleted already at 50 V. Consequently, the effective gap measured with the beam can be calculated as an average weighted with the squared standard deviations of the measured values. This average is $(443 \pm 3_{stat.} \pm 11_{syst.})$ µm. Here the smallest of the systematic error values was used, in order to obtain a conservative total systematic error.

By subtracting from this the value $(418 \pm 11_{stat.})$ µm of the gap measured on the metrology table, the sum of the average widths of the two insensitive layers at the edges of the sensors is $(25 \pm 12_{stat.} \pm 11_{syst.})$ µm.

If the insensitive layers have even and equal widths, their common value is one half of the above result, and the statistical error will be divided by $\sqrt{2}$, while the systematic error will be divided by 2. The dead layer thickness in this case is (12.5 ± 8 ± 6) µm. We can therefore conclude that the experimental thickness of the dead layer is compatible with zero within the statistical accuracy of 8 µm and within the systematic accuracy of 6 µm.

It is interesting to note that higher precision in determining the dead layer thickness would require improved precision in the edges straightness and parallelism and in its optical measurement. While the limited accuracy of the tracker can be compensated by large statistics, the systematic errors in the beam results would require a higher tracker resolution and better statistics, because smaller bins would be desirable in the data to be fitted. The errors due to chipped and non-parallel edges could be solved with *x-y* tracking, which would also require higher statistics to scan accurately the edge.